Microbubbles Loaded with Nanoparticles: A Route to Multiple Imaging Modalities

Jai Il Park,[†] Dinesh Jagadeesan,[†] Ross Williams,[‡] Wendy Oakden,[‡] Siyon Chung,[†] Greg J. Stanisz,[‡] and Eugenia Kumacheva[†,*]

[†]Department of Chemistry, University of Toronto, 80 Saint George Street, Toronto, ON, M5S3H6 Canada, and [‡]Sunnybrook Research Institute, Sunnybrook Health Sciences Centre, Toronto, 2075 Bayview Avenue, Toronto, ON, M4N 3M5 Canada

ABSTRACT We report a single-step approach to producing small and stable bubbles functionalized with nanoparticles. The strategy includes the following events occurring in sequence: (i) a microfluidic generation of bubbles from a mixture of CO_2 and a minute amount of gases with low solubility in water, in an aqueous solution of a protein, a polysaccharide, and anionic nanoparticles; (ii) rapid dissolution of CO_2 leading to the shrinkage of bubbles and an increase in acidity of the medium in the vicinity of the bubbles; and (iii) co-deposition of the biopolymers and nanoparticles at the bubble—liquid interface. The proposed approach yielded microbubbles with a narrow size distribution, long-term stability, and multiple functions originating from the attachment of metal oxide, metal, or semiconductor nanoparticles onto the bubble surface. We show the potential applications of these bubbles in ultrasound and magnetic resonance imaging.

KEYWORDS: microbubble · nanoparticles · interfaces · microfluidics · biomaterials · ultrasound · magnetic resonance imaging

Ultrasound (US) imaging is non-invasive, safe, and cost-effective;[1] however, in comparison with other imaging techniques, such as X-ray tomography or magnetic resonance imaging (MRI),[2] it has low contrast. To address this shortcoming, microbubbles are utilized as US imaging contrast agents. Microbubbles enhance backscattered acoustic signal, due to the large impedance mismatch between the bubbles and the living tissue, and enable resonant scattering.[1,3,4] Further improvement in the accuracy of clinical assessment of a disease can be achieved by combining US with other imaging modalities such as MRI or fluorescence imaging.[5−10] Multiple imaging modalities are realized by immobilizing magnetic or semiconductor nanoparticles (NPs) on the bubble surface.[9,10] Attachment of NPs to the bubble surface also increases the contrast in US imaging, owing to enhanced asymmetric bubble oscillations.[1,11] In addition to diagnostics, microbubbles carrying drug-loaded NPs have promising therapeutic applications: bubbles could be disrupted by a localized US to release therapeutic agents at the target site.[12−15]

Currently, microbubbles coated with NPs are produced in a multistep procedure by sonicating a mixture of NPs and oil in the presence of a gas and subsequently transferring the resulting bubbles into an aqueous medium.[9,16] Alternatively, NPs are attached to the surface of bubbles in a layer-by-layer (LbL) deposition process.[10,17] These time-consuming processes yield bubbles with dimensions in the size range between one micrometer and tens of micrometers and a broad distribution of sizes.[18] Recently, a microfluidic (MF) strategy enabled the synthesis of monodisperse NP-loaded bubbles *via* the formation of double emulsions;[19] however, the method required a very careful tuning of the surface energies at the gas−liquid and liquid−liquid interfaces.[19,20] In addition, the dimensions of bubbles exceeded 10 μm, the size utilized in US diagnostics or therapeutics.[21] Small (<10 μm) NP-coated bubbles were generated using a three-step regulation of pH in microchannels.[22] The method required a significant reduction in microchannel dimensions, which is expensive and/or time-consuming. No application of NP-coated bubbles in MRI imaging has been reported. The development of an efficient, single-step method for producing monodisperse microbubbles loaded with NPs is highly desirable.

Here we report a single-step MF approach to producing NP-coated microbubbles with a narrow size distribution and a long-term stability. The proposed approach exploits the following events, occurring concurrently within 3 s: (i) the MF generation of monodisperse bubbles from a mixture of CO_2 and a minute amount of a

*Address correspondence to ekumache@chem.utoronto.ca.

Received for review September 1, 2010 and accepted October 11, 2010.

Published online October 18, 2010. 10.1021/nn102248g

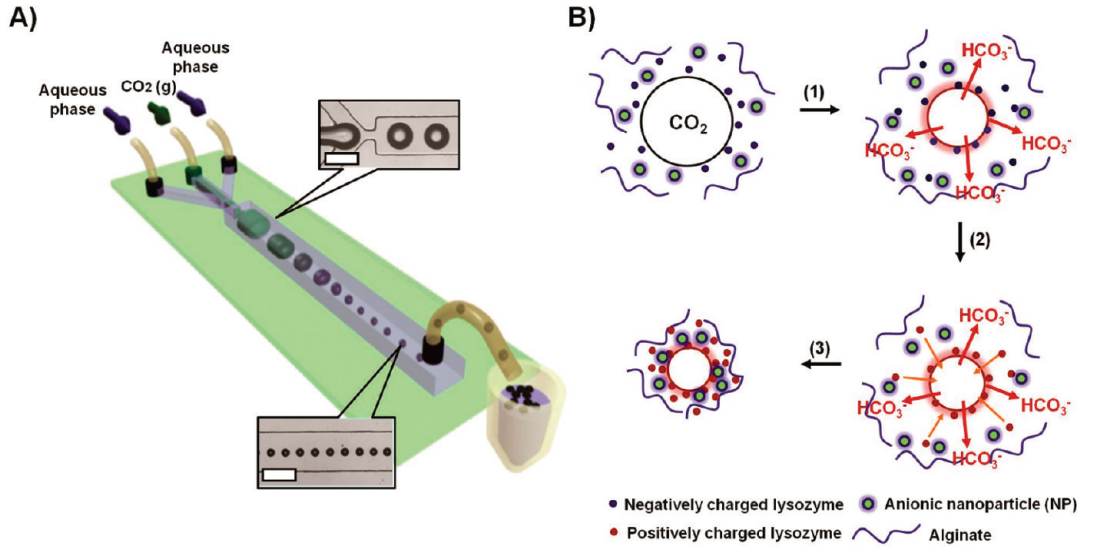

Figure 1. Microfluidic (MF) approach to the generation of NP-functionalized bubbles. (A) Schematic of the MF reactor. The height of the device is 120 μm; the width of the orifice and the length of the downstream microchannel are 50 μm and 260 mm, respectively. The top and the bottom insets show optical microcopy images of the bubbles at the beginning and the end of the process, respectively. Scale bars in the insets are 200 μm. (B) Schematic of the formation of NP-functionalized bubbles stabilized with a mixed lysozyme−alginate layer.

gas with a low solubility in water, in an aqueous solution of lysozyme, alginate, and anionic NPs; (ii) the controllable dissolution of CO_2 leading to bubble shrinkage and an increase in acidity of the medium in the neighborhood of the bubbles. The decrease in pH renders positive net charge to lysozyme; and (iii) the adsorption of cationic lysozyme to the negatively charged surface of bubbles followed by the deposition of anionic alginate and NPs onto the lysozyme layer. This rapid and simple process generates bubbles with polydispersity not exceeding 6% and stability of at least 3 months. We show the ability to produce 5 μm diameter bubbles; however, for convenience of optical imaging, we present most of the results for bubbles with a mean diameter of approximately 10 μm. Bubbles with such dimensions, comparable to red blood cells, can safely pass through the microvasculature without diffusing across the endothelium.[23] We demonstrate the generality of the MF approach by attaching to the bubble surface metal oxide, metal, and semiconductor NPs. Furthermore, we show the applications of the NP-functionalized bubbles as imaging agents in US, fluorescence, and MRI.

RESULTS AND DISCUSSION

Figure 1A shows the schematic of the MF device used in the present work. A MF flow-focusing bubble generator[24] is followed by a serpentine downstream microchannel channel (Figure S1, Supporting Information). The CO_2 gas mixed with 0.2 vol % of N_2, O_2, He, and Ne is supplied under pressure P_{CO_2} of 48.3 kPa to the central channel. The aqueous solution containing a mixture of lysozyme, alginate, and anionic NPs (Fe_3O_4, Au, or SiO_2-encapsulated CdSe/ZnS NPs) is introduced into the two side channels using a syringe pump at the flow rate, Q_L, varying from 6.5 to 9.5 mL/h. The initial value of pH = 12 of the continuous aqueous phase is achieved by adding a 1 M NaOH solution to the continuous aqueous phase. Formation of bubbles occurs *via* a periodic breakup of the gas thread in the orifice of the MF device.[24] Since the unperturbed diameter of the bubbles immediately after their formation is larger than the height of the downstream channel, they acquire a discoid shape (Figure 1A, top inset). In the downstream channel, the dimensions of the bubbles dramatically reduce, due to the dissolution of CO_2, and acquire a spherical shape (Figure 1A, bottom inset).

Figure 1B illustrates the sequence of events leading to the generation of small and stable NP-functionalized bubbles encapsulated with the mixture of biopolymers. Rapid and uniform shrinkage of bubbles is driven by the dissolution of CO_2 and chemical reactions of CO_2 with OH^- ions (see below). The dissolution of CO_2 leads to the decrease in pH of the aqueous medium in the vicinity of the gas−liquid interface (Figure 1B(1)). As a result of the change in acidity, lysozyme molecules in the neighborhood of the bubbles gain a net positive charge and adsorb to the negatively charged bubble surface (Figure 1B(2)) (the isoelectric point of lysozyme is ~11).[25,26] Anionic NPs and anionic alginate molecules deposit on the cationic lysozyme-coated bubble, due to electrostatically mediated attraction (Figure 1B(3)), so that the NPs are predominantly localized between the lysozyme and alginate shells.

An important feature of our work was the ability to control the dimensions of bubbles, which was achieved by generating bubbles with a well-defined size, controllable dissolution of CO_2, and stabilization of the bubbles with a biopolymer layer. The dissolution of CO_2 in the microchannel was governed by Henry's law (eq 1),

which was combined with chemical reactions occurring at pH > 10 (eqs 2 and 3):[27]

$$[CO_2]_l = k_H P_{CO_2} \quad (1)$$

$$CO_2 + OH^- \overset{K_1}{\leftrightarrow} HCO_3^- \quad (2)$$

$$HCO_3^- + OH^- \overset{K_2}{\leftrightarrow} CO_3^{2-} + H_2O \quad (3)$$

where $K_1 = 3.2 \times 10^7$ and $K_2 = 3.5 \times 10^3$ are the equilibrium constants and $[CO_2]_l$, k_H, and P_{CO_2} are the concentration of molecularly dissolved CO_2, Henry's law constant (for CO_2 at 25 °C, $k_H = 3.2 \times 10^{-4}$ mol/(L kPa)), and the gas pressure, respectively. The extent of dissolution of bubbles in the MF device was controlled by the saturation of the continuous aqueous phase,[28] and in the present work, the dissolution led to ~80% of the reduction in bubble volume.

The bubbles were generated at a frequency of 700 bubbles/s. The biopolymer-encapsulated NP-loaded bubbles were collected in a 2 mL container, where their dimensions further decreased due to the reduction of external pressure to 1 atm.[29,30] The container was sealed for long-term bubble storage.

Figure 2A−C shows typical optical microscopy images taken at different times after the generation of biopolymer-encapsulated bubbles coated with Fe_3O_4 NPs. The polydispersity of the bubbles did not exceed 6%. Following bubble formation, within 3 s, their mean diameter reduced from 150 to 40 μm (on-chip) and, subsequently, to 5 μm within 1 h of off-chip storage. At this point, the fractional reduction in the bubble volume reached 99.9%, which implied that all CO_2 and 0.1% of the low-soluble gases were removed from the bubbles. No further change in bubble dimensions was observed after 2000 h storage.

The final dimensions of bubbles—defined as the diameter of bubbles after 1 h storage—were tuned by varying the value of Q_L of the continuous aqueous phase. Figure 2D shows the variation in the initial (D_i) and the final (D_f) dimensions of NP-coated bubbles, plotted as a function of the Q_L of the continuous phase. The value of Q_L affected the final size of bubbles in two ways. With increasing value of Q_L, the original bubble size reduced, thereby resulting in the decrease of D_f. Second, the extent of dissolution of CO_2 increased at higher values of Q_L,[28,31] also leading to smaller bubble size (Figure S2, Supporting Information).

We conducted a series of control experiments. When the bubbles were generated in the absence of lysozyme, they were completely dissolved within a few minutes after their generation. Without alginate in the continuous phase, the bubbles aggregated due to insufficient electrostatic and steric stabilization (Figure S3A, Supporting Information). The importance of local acidification of the medium was examined by generating N_2 bubbles at pH = 12. These bubbles did not have

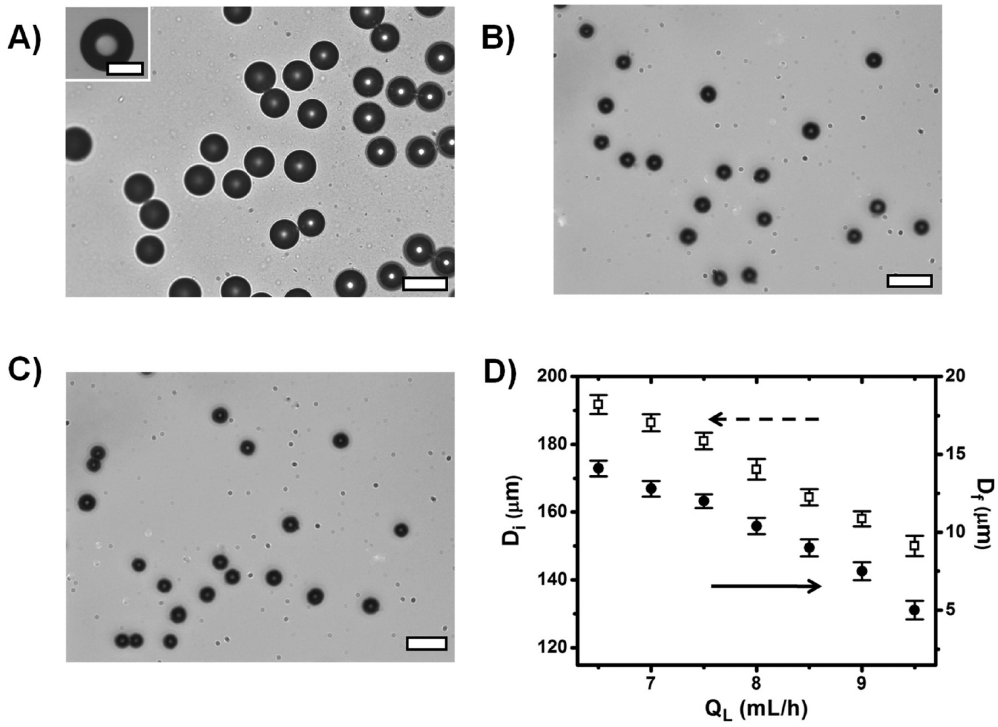

Figure 2. Optical microscopy images of the bubbles functionalized with Fe_3O_4 NPs after different storage times: (A) 3 s, (B) 1 h, and (C) 2000 h. The scale bars in A, B, and C are 50, 15, and 15 μm, respectively. Inset in A shows the bubble imaged immediately after its generation in the orifice of the MF device. Scale bar is 100 μm. Bubbles were generated at P_{CO_2} = 48.3 kPa and Q_L = 9.5 mL/h. (D) Variations in the initial (D_i) and final dimensions (D_f) of microbubbles are plotted as a function of the flow rate of the continuous phase; P_{CO_2} = 48.3 kPa.

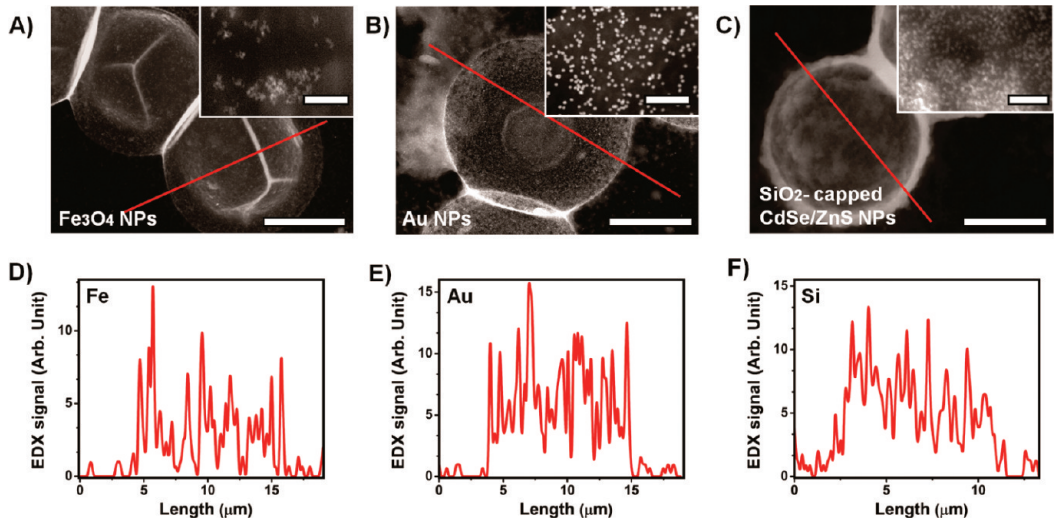

Figure 3. Scanning transmission electron microscopy (STEM) images of the bubbles coated with the lysozyme−alginate shell and (A) Fe_3O_4 NPs, (B) Au NPs, and (C) SiO_2-encapsulated CdSe/ZnS NPs. Scale bars are 6 μm. Insets in A−C show corresponding high-magnification images of the surface of the bubbles. Scale bars in the insets are 150 nm. (D−F) Energy-dispersive X-ray (EDX) spectrometry line scanning profiles for the system shown as a red line in A−C. Bubbles were generated at P_{CO_2} = 48.3 kPa and Q_L = 8.5 mL/h.

a dense lysozyme−alginate shell, and within 1 h, they underwent coalescence (Figure S3B, Supporting Information). We also found that, without biopolymers, the deposition of, for example, Fe_3O_4 NPs alone, did not lead to the formation of a dense stabilizing NP layer on the bubble surface, in contrast to our previous work conducted with micrometer-size particles.[32] The results of control experiments imply that the size and the surface properties of Fe_3O_4 NPs were not suitable for bubble stabilization, and the approach described in the present paper is more general. The combination of biopolymer layers and NPs was required in order to realize multiple imaging modalities in biological environments. In addition, the ability to bioconjugate biopolymers in the bubble shell could benefit in the targeted (site-specific) drug delivery.

The NP-coated bubbles were washed several times with deionized water, dried, and imaged using scanning transmission electron microscopy (STEM). The STEM images of the bubbles coated with Fe_3O_4, Au, and SiO_2-encapsulated CdSe/ZnS NPs are shown in Figure 3A−C, respectively. We note that the CdSe/ZnS NPs were encapsulated within a SiO_2 shell in order to suppress the cytotoxicity of these NPs.[33] Upon drying, the bubbles maintained a spherical shape and featured wrinkles on their surface. In the high-magnification images (insets in Figure 3A−C), the NPs appeared bright on the dark background of the lysozyme−alginate biopolymer shell. The Au and SiO_2-encapsulated CdSe/ZnS NPs were well-separated; however, Fe_3O_4 NPs tend to form clusters in the biopolymer shells.

In each system, the presence of NPs on the surface of bubbles was verified by energy-dispersive X-ray (EDX) analysis. Figure 3D−F shows the results of EDX analysis of the surface of bubbles, based on the major constituent of the NPs. The EDX line profiles featured strong EDX signals of Fe, Au, and Si (see also Figures S4−S6, Supporting Information).

Control over the amount of NPs deposited on the surface of bubbles was achieved by varying the concentration of NPs in the continuous phase. Figure 4A−C shows the STEM images of the surface of bubbles coated with a different amount of Fe_3O_4 NPs. When the initial concentration of the NPs in the continuous phase was 1.0×10^{12}, 4.0×10^{12}, or 1.0×10^{13} NPs/mL, their density on the surface of bubbles was 1.5×10^5, 6.6×10^5, and 1.5×10^7 NPs/μm^2, respectively (Figure 4A−C).

Properties of NP-Functionalized Bubbles. The NP-functionalized bubbles had a narrow size distribution:

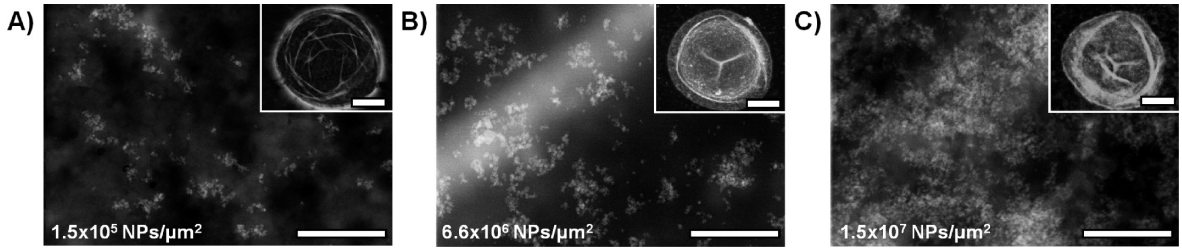

Figure 4. (A−C) STEM images of the surface of bubbles coated with Fe_3O_4 NPs at a surface density of (A) 1.5×10^5, (B) 6.6×10^5, and (C) 1.5×10^6 NPs/μm^2. The concentration of NPs in the polymer shell was determined using ICP-AES. Scale bars are 300 nm. Insets show the corresponding bubbles. Scale bars are 3 μm. Bubbles were generated at P_{CO_2} = 48.3 kPa and Q_L = 8 mL/h.

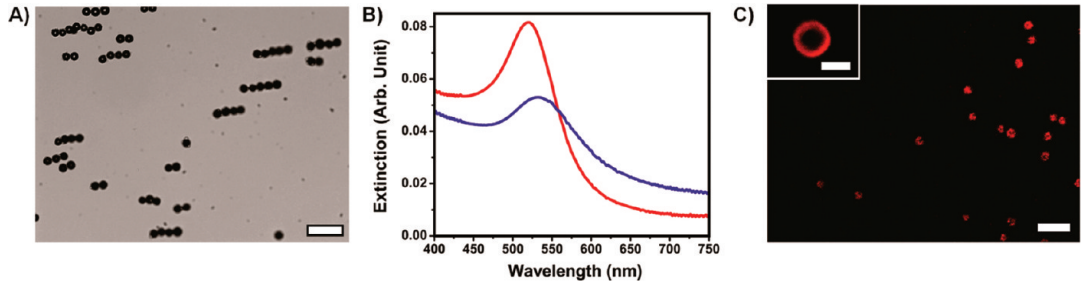

Figure 5. Properties of NP-coated bubbles. (A) Magnetic actuation of bubbles functionalized with Fe_3O_4 NPs. Scale bar is 50 μm. Bubbles were generated at P_{CO_2} = 48.3 kPa and Q_L = 8.5 mL/h. (B) Extinction spectra of Au NPs (red spectrum) and of the bubbles coated with these Au NPs (blue spectrum). Bubbles were generated at P_{CO_2} = 48.3 kPa and Q_L = 8.5 mL/h. (C) Confocal fluorescence microscopy image of bubbles carrying SiO_2-encapsulated CdSe/ZnS NPs. Scale bar is 30 μm; λ_{ex} = 364 nm. Inset shows an image of the individual bubble. Scale bar is 5 μm. Bubbles were generated at P_{CO_2} = 48.3 kPa and Q_L = 9.5 mL/h.

their polydispersity did not exceed 6%. The thickness of the shell was approximately 1 μm, based on the results of confocal image analyses (Figure S7, Supporting Information). The bubbles coated with Fe_3O_4 NPs were readily aligned in chains when manipulated by an external magnetic field (Figure 5A).[34] The chains of bubbles moved toward a magnet at a velocity of ~20 μm/s. The bubbles did not lose their ability for magnetic actuation for at least 3 month-long storage (Figure S8, Supporting Information).

Figure 5B shows the extinction spectra of the aqueous dispersion of bubbles coated with Au NPs and of the original citrate-stabilized Au NPs in an aqueous solution. The incorporation of Au NPs within a biopolymer shell led to a ~13 nm red shift of the surface plasmon resonance bands, due to interparticle electromagnetic coupling.[35,36]

Figure 5C shows a typical confocal fluorescence microscopy image of the bubbles coated with SiO_2-encapsulated CdSe/ZnS NPs. The shell of bubbles showed strong fluorescence when excited at 364 nm (Figure S9, Supporting Information). Figure 5C inset shows a gaseous core (dark) and a bright fluorescent shell of an individual bubble.

Application of NP-Functionalized Bubbles in US Imaging. Aqueous dispersions of the bubbles were introduced in the Opticell chamber (Thermoscientific Inc.) and imaged in a bubble-specific, nonlinear imaging mode using a clinical US system (iU22, Philips). The nonlinear US signal was caused by asymmetric (compression *vs* expansion) oscillations of the bubbles in response to US excitation. Figure 6A−D shows *in vitro* US images of the dispersion of NP-free and NP-functionalized bubbles. A stronger contrast in US images in Figure 6A−D signified a stronger nonlinear signal enhancement for the NP-functionalized bubbles, in comparison with NP-free bubbles. Quantitatively, signal enhancement for the NP-coated bubbles is presented in Figure 6E. The signals of the bubble dispersions were compared to the background signal of water. The enhancement was calculated as the ratio of the integrated power measured in the chamber filled with the dispersion of bubbles to the integrated power measured for the chamber containing pure water. The bubbles functionalized with Fe_3O_4, Au, and SiO_2-encapsulated CdSe/ZnS NPs showed 24.1, 32.7, and 34 dB signal enhancements,

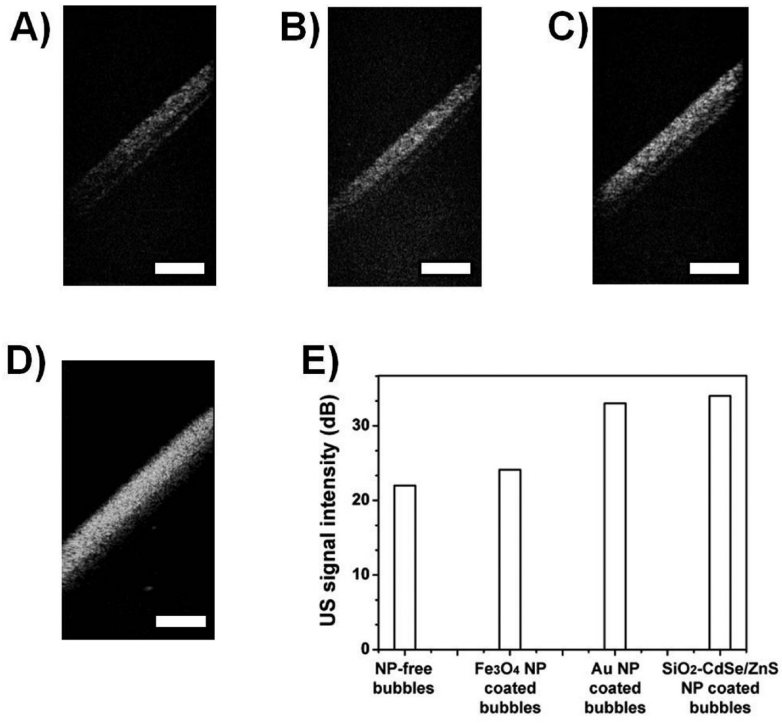

Figure 6. *In vitro* US imaging of the dispersion of biopolymer-coated bubbles at 90% receive gain. The dispersion is placed in the Opticell chamber. (A) NP-free bubbles, bubbles coated with (B) Fe_3O_4 NPs, (C) Au NPs, and (D) SiO_2-encapsulated CdSe/ZnS NPs. (E) US signal enhancement over background for the systems shown in A−D. Scale bars are 5 mm. The concentration of bubbles in all systems was 10^4 bubbles/mL.

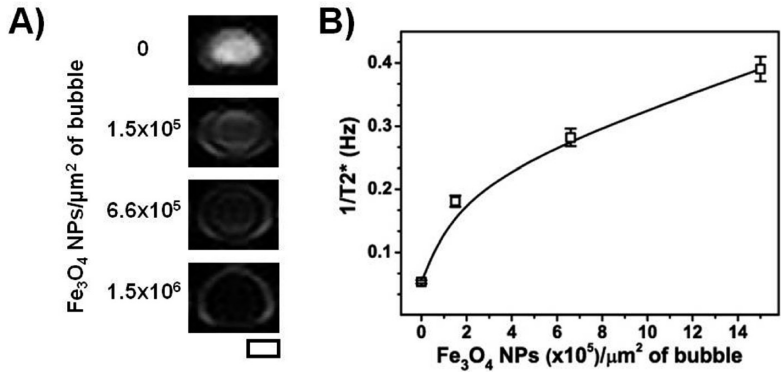

Figure 7. (A) *In vitro* MRI images (top view) of the dispersions of biopolymer-encapsulated bubbles coated with different amounts of Fe_3O_4 NPs. The images were obtained at 6.9 ms echo time. Scale bar is 5 mm. (B) Variation in T_2* relaxation rate plotted as a function of surface density of Fe_3O_4 NPs on the surface of bubbles. The concentration of bubbles in all systems was 10^4 bubbles/mL.

respectively, in comparison with 21.7 dB enhancement measured for the NP-free bubbles (Figures 6E). We ascribe the increase in the US signal to the enhanced nonlinearity in oscillations of the NP-coated bubbles, owing to the increased microbubble resistance to compression.[11,16,37] The stronger nonlinear US signal measured for the bubbles carrying Au or SiO_2-encapsulated CdSe/ZnS NPs, in comparison with the bubbles carrying Fe_3O_4 NPs, supports this explanation. On the basis of the STEM image analyses (Figure 3A−C, insets), the surface coverage of the bubbles with Au and SiO_2-encapsulated CdSe/ZnS NPs was 3- and 5-fold higher, respectively, than that for the bubbles coated with Fe_3O_4 NPs. We conclude that the deposition of NPs onto the bubble surface increased the detectability of bubbles with contrast-specific US pulse sequences which were designed to reject the linear signal components arising from the tissue and bubbles and to preserve the nonlinear components from the bubbles.[1,37]

The NP-coated bubbles did not lose their echogenicity under continuous exposure to low-power US pulses (130 kPa at 5 MHz), suggesting an excellent stability of the lysozyme−alginate shell with embedded NPs. Under increased peak negative US pressure of 1100 kPa, the bubbles were disrupted. This result implied that the NP-loaded bubbles can be controllably disrupted with US, and the NPs can be released and deposited at the target sites under US image guidance.

Application of NP-Functionalized Bubbles in MRI. We examined the application of the Fe_3O_4 NP-coated bubbles in MRI, a method providing a high spatial resolution. The NP-coated bubbles with the surface density of 0, 1.5 × 10^5, 6.6 × 10^5, and 1.5 × 10^6/μm^2 were suspended in water and placed in 2 mL Eppendorf tubes. The dispersions were imaged at 3.0 T with a 2D coronal fast field echo sequence (Philips Healthcare, Andover, MA). Figure 7A shows that the bubbles carrying a higher amount of Fe_3O_4 NPs exhibited enhanced negative contrast, reflected as the darker area in the center of the Eppendorf tubes.[38,39] Figure 7B shows the increase in relaxation rate ($1/T_2$*) for dispersions containing bubbles with a higher surface density of Fe_3O_4 NPs. The NPs modified the MRI signal by locally perturbing the magnetic field and thereby leading to the negative signal enhancement by increasing the T_2* relaxation rate of the nearby water molecules.[39,40] These results indicate that the Fe_3O_4 NP-coated bubbles can serve as effective MRI contrast agents.

CONCLUSIONS

In conclusion, we have developed a single-step, simple method for producing microbubbles functionalized with various types of NPs. The bubbles exhibit small size, a low polydispersity, and long-term stability. The functionalization of the surface of bubbles rendered the bubbles with plasmonic, fluorescence, and magnetic properties. The NP-coated bubbles showed enhanced performance in US imaging. We also demonstrated multiple imaging modalities for NP-functionalized bubbles, such as fluorescence and MRI. We envisage that these multifunctional bubbles will have important applications in medical diagnostics where multiple imaging methods using a single contrast agent will be advantageous. The proposed method can also be used in triggered site-specific release of drugs by using magnetic actuation and focused US exposure.

METHODS

Materials. CO_2 (purity 99.8%) was purchased from BOC Canada. Impurities included N_2, O_2, and inert gases such as He and Ne. Alginic acid sodium salt (alginate) and hen egg white lysozyme (lysozyme) were purchased from Sigma-Aldrich Canada and used as received. Sodium hydroxide (NaOH, EMD Canada) was used to adjust the pH of the aqueous lysozyme and alginate solutions. Fe_3O_4 NPs coated with poly(acrylic acid) were purchased from Chemicell, Germany. Citrate-stabilized gold NPs and SiO_2-encapsulated CdSe/ZnS NPs were synthesized as previously described.[33,41]

Fabrication of MF Device. Photolithographic masters were prepared from SU-8 50 photoresist (MicroChem) in bas-relief on silicon wafers. The MF bubble generators used in the present work were fabricated in poly(dimethyl siloxane) (Sylgard 184, Dow Corning), using a standard soft lithography procedure.[42]

Characterization. An Olympus BX51 microscope built with a high-speed camera (Photometrics CoolSNAP ES) was used to image the bubbles. An Image Pro (Media Cybernetics) software was used to determine the dimension and polydispersity (defined as standard deviation in bubble diameter divided by its mean diameter) of bubbles. The volume, V, of an unperturbed

spherical bubble was calculated as $V = (4/3)\pi(D/2)^3$, where D is the diameter of the bubble. When the value of D is larger than the height, $h = 120$ μm, of the microchannel, the volume of bubbles was calculated as $V = (\pi/12)[2D^3 - (D - h)^2(2D + h)]$.[43]

Hitachi HD-2000 scanning transmission electron microscopy (STEM) was used to image the surface of NP-functionalized bubbles. After 24 h storage, they were washed with deionized water several times and dried on the grid prior to imaging. Laser confocal fluorescence microscopy (Zeiss LSM 510 Meta microscope equipped with an Axiovert 200 M microscope, λ_{ex}= 364 nm) was used to examine the photoluminescence of NP-free and NP-loaded bubbles encapsulated with the biopolymer shell.

Inductively coupled plasma atomic emission spectroscopy (ICP-AES) was used to determine the concentration of Fe_3O_4 NPs on the surface of the bubble after 24 h storage. The amount of Fe in the bubbles was estimated as follows: $C_{bubbles(Fe)} = C_{initial(Fe)} - C_{final(Fe)}$, where $C_{bubbles(Fe)}$ is the concentration of Fe in the suspension of bubbles (g/mL), $C_{initial(Fe)}$ and $C_{final(Fe)}$ are the initial and final concentrations of Fe in the continuous phase (g/mL), respectively. The number of NPs per bubble was estimated as $C_{bubbles(Fe)} \times MW_{Fe_3O_4}/(3 \times MW_{Fe} \times d \times V \times N)$, where $MW_{Fe_3O_4}$ and MW_{Fe} are the molecular weight of Fe (55.8 g/mol) and Fe_3O_4 (231.5 g/mol), respectively; d and V are the density (~1.25 g/mL) and volume (~4.2×10^{-18} mL) of the NP, respectively. N is the number concentration of bubbles (~10^6 bubbles/mL).

The plasmonic spectra were monitored by measuring absorption spectra of aqueous dispersions of gold NPs and bubbles loaded with gold NPs using a Varian Cary 5000 UV−vis spectrometer. The intensity profiles of fluorescence emission for SiO_2-capped CdSe/ZnS NPs, bubbles encapsulated with the biopolymers embedded with and without the NPs dispersed in water were measured at λ_{ex} = 364 nm (Cary Eclipse, Varian).

***In Vitro* US Imaging Experiments.** Ten milliliters of the bubble suspension with a concentration of approximately 10^4 bubbles/mL was introduced into Opticell chamber (Thermoscientific Inc.). The bubbles were exposed to a focused ultrasound pulse (5 MHz) using L9-3 transducer and iU22 ultrasound system (Philips). *In vitro* US images were obtained using a bubble-specific, nonlinear imaging mode. The signal enhancement values were obtained by examining a 5 mm × 5 mm region of interest and recording the average integrated power within this region for the contrast-specific (nonlinear mode) image.

***In Vitro* MRI Experiments.** Dispersions of bubbles with a bubble concentration of 10^4 bubbles/mL and with varying amount of Fe_3O_4 NPs on the bubble surface were introduced into 2 mL Eppendorf tubes. The tubes were placed in a plastic holder and submerged in water to eliminate unwanted external susceptibility effects arising from air−water interfaces, which would also cause a signal decrease on T_2-weighted images. Imaging was conducted using a Philips Achieva 3.0T MRI scanner (Philips Healthcare, Andover, MA) with a 2D coronal fast field echo sequence (parameters: 128 mm field of view, 1 mm × 1 mm × 5 mm resolution, repetition time 100 ms, flip angle 15°, and four different echo times: 4.6, 6.9, 9.2, and 20.7 ms). T_2* values were fit to these data using MatLab (The MathWorks, Inc., Natick, MA).

Acknowledgment. The authors thank I. Gorelikov, I. Gourevich, N. Matsuura, M. Seo, K. Liu, and J. Vickery for assistance in the experiments, and P. Burns for material support in the US imaging experiments. E.K. thanks NSERC Canada for financial support of this work.

Supporting Information Available: Details for MF experiments and bubble characterization. This material is available free of charge *via* the Internet at http://pubs.acs.org.

REFERENCES AND NOTES

1. Schutt, E. G.; Klein, D. H.; Mattrey, R. M.; Riess, J. G. Injectable Microbubbles as Contrast Agents for Diagnostic Ultrasound Imaging: The Key Role of Perfluorochemicals. *Angew. Chem., Int. Ed.* **2003**, *42*, 3218–3235.
2. Cosgrove, D. Ultrasound Contrast Agents: An Overview. *Eur. J. Radiol.* **2006**, *60*, 324–330.
3. Lentacker, I.; De Smedt, S. C.; Sanders, N. N. Drug Loaded Microbubble Design for Ultrasound Triggered Delivery. *Soft Matter* **2009**, *5*, 2161–2170.
4. Lindner, J. R. Microbubbles in Medical Imaging: Current Applications and Future Directions. *Nat. Rev. Drug Discovery* **2004**, *3*, 527–532.
5. Dharmakumar, R.; Plewes, D. B.; Wright, G. A. A Novel Microbubble Construct for Intracardiac or Intravascular MR Manometry: A Theoretical Study. *Phys. Med. Biol.* **2005**, *50*, 4745–4762.
6. Huh, Y. M.; Jun, Y. W.; Song, H. T.; Kim, S.; Choi, J. S.; Lee, J. H.; Yoon, S.; Kim, K. S.; Shin, J. S.; Suh, J. S.; *et al. In Vivo* Magnetic Resonance Detection of Cancer by Using Multifunctional Magnetic Nanocrystals. *J. Am. Chem. Soc.* **2005**, *127*, 12387–12391.
7. Medintz, I. L.; Uyeda, H. T.; Goldman, E. R.; Mattoussi, H. Quantum Dot Bioconjugates for Imaging, Labelling and Sensing. *Nat. Mater.* **2005**, *4*, 435–446.
8. Mulder, W. J. M.; Koole, R.; Brandwijk, R. J.; Storm, G.; Chin, P. T. K.; Strijkers, G. J.; Donega, C. D.; Nicolay, K.; Griffioen, A. W. Quantum Dots with a Paramagnetic Coating as a Bimodal Molecular Imaging Probe. *Nano Lett.* **2006**, *6*, 1–6.
9. Yang, F.; Li, Y. X.; Chen, Z. P.; Zhang, Y.; Wu, J. R.; Gu, N. Superparamagnetic Iron Oxide Nanoparticle-Embedded Encapsulated Microbubbles as Dual Contrast Agents of Magnetic Resonance and Ultrasound Imaging. *Biomaterials* **2009**, *30*, 3882–3890.
10. Ke, H.; Xing, Z. W.; Zhao, B.; Wang, J. R.; Liu, J. B.; Guo, C. X.; Yue, X. L.; Liu, S. Q.; Tang, Z. Y.; Dai, Z. F. Quantum-Dot-Modified Microbubbles with Bi-Mode Imaging Capabilities. *Nanotechnology* **2009**, *20*, 1–8.
11. Stride, E.; Pancholi, K.; Edirisinghe, M. J.; Samarasinghe, S. Increasing the Nonlinear Character of Microbubble Oscillations at Low Acoustic Pressures. *J. R. Soc. Interface* **2008**, *5*, 807–811.
12. Cavalieri, F.; Finelli, I.; Tortora, M.; Mozetic, P.; Chiessi, E.; Polizio, F.; Brismar, T. B.; Paradossi, G. Polymer Microbubbles as Diagnostic and Therapeutic Gas Delivery Device. *Chem. Mater.* **2008**, *20*, 3254–3258.
13. Lentacker, I.; De Smedt, S. C.; Demeester, J.; Van Marck, V.; Bracke, M.; Sanders, N. N. Lipoplex-Loaded Microbubbles for Gene Delivery: A Trojan Horse Controlled by Ultrasound. *Adv. Funct. Mater.* **2007**, *17*, 1910–1916.
14. Lum, A. F. H.; Borden, M. A.; Dayton, P. A.; Kruse, D. E.; Simon, S. I.; Ferrara, K. W. Ultrasound Radiation Force Enables Targeted Deposition of Model Drug Carriers Loaded on Microbubbles. *J. Controlled Release* **2006**, *111*, 128–134.
15. Postema, M.; Gilja, O. H. Ultrasound-Directed Drug Delivery. *Curr. Pharm. Biotechnol.* **2007**, *8*, 355–361.
16. Yang, F.; Li, L.; Li, Y. X.; Chen, Z. P.; Wu, J. R.; Gu, N. Superparamagnetic Nanoparticle-Inclusion Microbubbles for Ultrasound Contrast Agents. *Phys. Med. Biol.* **2008**, *53*, 6129–6141.
17. Cavalieri, F.; Ashokkumar, M.; Grieser, F.; Caruso, F. Ultrasonic Synthesis of Stable, Functional Lysozyme Microbubbles. *Langmuir* **2008**, *24*, 10078–10083.
18. Stride, E.; Edirisinghe, M. Novel Microbubble Preparation Technologies. *Soft Matter* **2008**, *4*, 2350–2359.
19. Lee, M. H.; Prasad, V.; Lee, D. Microfluidic Fabrication of Stable Nanoparticle-Shelled Bubbles. *Langmuir* **2010**, *26*, 2227–2230.
20. Shum, H. C.; Kim, J. W.; Weitz, D. A. Microfluidic Fabrication of Monodisperse Biocompatible and Biodegradable Polymersomes with Controlled Permeability. *J. Am. Chem. Soc.* **2008**, *130*, 9543–9549.
21. Hettiarachchi, K.; Talu, E.; Longo, M. L.; Dayton, P. A.; Lee, A. P. On-Chip Generation of Microbubbles as a Practical Technology for Manufacturing Contrast Agents for Ultrasonic Imaging. *Lab Chip* **2007**, *7*, 463–468.
22. Seo, M.; Gorelikov, I.; Williams, R.; Matsuura, N. Microfluidic Assembly of Monodisperse, Nanoparticle-Incorporated Perfluorocarbon Microbubbles for Medical Imaging and Therapy. *Langmuir* **2010**, *26*, 13855–13860.

23. Mayer, S.; Grayburn, P. A. Myocardial Contrast Agents: Recent Advances and Future Directions. *Prog. Cardiovasc. Dis.* **2001**, *44*, 33–44.
24. Garstecki, P.; Gitlin, I.; DiLuzio, W.; Whitesides, G. M.; Kumacheva, E.; Stone, H. A. Formation of Monodisperse Bubbles in a Microfluidic Flow-Focusing Device. *Appl. Phys. Lett.* **2004**, *85*, 2649–2651.
25. Takahashi, M. ζ Potential of Microbubbles in Aqueous Solutions: Electrical Properties of the Gas−Water Interface. *J. Phys. Chem. B* **2005**, *109*, 21858–21864.
26. Krebs, M. R. H.; Devlin, G. L.; Donald, A. M. Protein Particulates: Another Generic Form of Protein Aggregation. *Biophys. J.* **2007**, *92*, 1336–1342.
27. Danckwerts, P. V. *Gas-Liquid Reactions*; McGraw-Hill Book Company: New York, 1970.
28. Park, J. I.; Nie, Z. H.; Kumachev, A.; Kumacheva, E. A Microfluidic Route to Small CO_2 Microbubbles with Narrow Size Distribution. *Soft Matter* **2010**, *6*, 630–634.
29. CO_2 bubbles experienced a pressure of 48.3 kPa in the microchannel, while partial CO_2 pressure at 1 atm (outside the device) is 0.04 kPa (see ref 30).
30. Persat, A.; Chambers, R. D.; Santiago, J. G. Basic Principles of Electrolyte Chemistry for Microfluidic Electrokinetics. Part I: Acid−Base Equilibria and pH Buffers. *Lab Chip* **2009**, *9*, 2437–2453.
31. Park, J. I.; Tumarkin, E.; Kumacheva, E. Small, Stable, and Monodispersed Bubbles Encapsulated with Biopolymers. *Macromol. Rapid Commun.* **2010**, *31*, 222–227.
32. Park, J. I.; Nie, Z.; Kumachev, A.; Abdelrahman, A. I.; Binks, B. P.; Stone, H. A.; Kumacheva, E. A Microfluidic Approach to Chemically Driven Assembly of Colloidal Particles at Gas−Liquid Interfaces. *Angew. Chem., Int. Ed.* **2009**, *48*, 5300–5304.
33. Selvan, S. T.; Tan, T. T.; Ying, J. Y. Robust, Non-cytotoxic, Silica-Coated CdSe Quantum Dots with Efficient Photoluminescence. *Adv. Mater.* **2005**, *17*, 1620–1625.
34. Erb, R. M.; Son, H. S.; Samanta, B.; Rotello, V. M.; Yellen, B. B. Magnetic Assembly of Colloidal Superstructures with Multipole Symmetry. *Nature* **2009**, *457*, 999–1002.
35. Lu, Z. D.; Goebl, J.; Ge, J. P.; Yin, Y. D. Self-Assembly and Tunable Plasmonic Property of Gold Nanoparticles on Mercapto-Silica Microspheres. *J. Mater. Chem.* **2009**, *19*, 4597–4602.
36. Zhang, D. M.; Neumann, O.; Wang, H.; Yuwono, V. M.; Barhoumi, A.; Perham, M.; Hartgerink, J. D.; Wittung-Stafshede, P.; Halas, N. J. Gold Nanoparticles Can Induce the Formation of Protein-Based Aggregates at Physiological pH. *Nano Lett.* **2009**, *9*, 666–671.
37. Stride, E. Physical Principles of Microbubbles for Ultrasound Imaging and Therapy. *Cerebrovasc. Dis.* **2009**, *27*, 1–13.
38. Bulte, J. W. M.; Kraitchman, D. L. Monitoring Cell Therapy Using Iron Oxide MR Contrast Agents. *Curr. Pharm. Biotechnol.* **2004**, *5*, 567–584.
39. Gao, J. H.; Liang, G. L.; Cheung, J. S.; Pan, Y.; Kuang, Y.; Zhao, F.; Zhang, B.; Zhang, X. X.; Wu, E. X.; Xu, B. Multifunctional Yolk-Shell Nanoparticles: A Potential MRI Contrast and Anticancer Agent. *J. Am. Chem. Soc.* **2008**, *130*, 11828–11833.
40. Pathak, A. P. Magnetic Resonance Susceptibility Based Perfusion Imaging of Tumors Using Iron Oxide Nanoparticles. *WIREs Nanomed. Nanobiotechnol.* **2009**, *1*, 84–97.
41. Enustun, B. V.; Turkevich, J. Coagulation of Colloidal Gold. *J. Am. Chem. Soc.* **1963**, *85*, 3317–3328.
42. Xia, Y. N.; Whitesides, G. M. Soft Lithography. *Annu. Rev. Mater. Sci.* **1998**, *28*, 153–184.
43. Nie, Z. H.; Seo, M. S.; Xu, S. Q.; Lewis, P. C.; Mok, M.; Kumacheva, E.; Whitesides, G. M.; Garstecki, P.; Stone, H. A. Emulsification in a Microfluidic Flow-Focusing Device: Effect of the Viscosities of the Liquids. *Microfluid. Nanofluid.* **2008**, *5*, 585–594.